

# Use of Hot Rolling for Generating Low Deviation Twins and a Disconnected Random Boundary Network in Inconel 600 Alloy



SANDEEP SAHU, PRABHAT CHAND YADAV, and SHASHANK SHEKHAR

In this investigation, Inconel 600 alloy was thermomechanically processed to different strains *via* hot rolling followed by a short-time annealing treatment to determine an appropriate thermomechanical process to achieve a high fraction of low- $\Sigma$  CSL boundaries. Experimental results demonstrate that a certain level of deformation is necessary to obtain effective “grain boundary engineering”; *i.e.*, the deformation must be sufficiently high to provide the required driving force for postdeformation static recrystallization, yet it should be low enough to retain a large fraction of original twin boundaries. Samples processed in such a fashion exhibited 77 pct length fraction of low- $\Sigma$  CSL boundaries, a dominant fraction of which was from  $\Sigma 3$  (~ 64 pct), the latter with very low deviation from its theoretical misorientation. The application of hot rolling also resulted in a very low fraction of  $\Sigma 1$  (~ 1 pct) boundaries, as desired. The process also leads to so-called “triple junction engineering” with the generation of special triple junctions, which are very effective in disrupting the connectivity of the random grain boundary network.

<https://doi.org/10.1007/s11661-017-4431-0>

© The Minerals, Metals & Materials Society and ASM International 2017

## I. INTRODUCTION

GRAIN boundaries play an important role in determining physical properties of polycrystalline materials. A number of studies have shown that intergranular degradation and failure depend strongly on grain boundary energy: the higher the energy, the higher is the susceptibility of grain boundary to promote intergranular degradation *via* cracking, cavitation, corrosion, segregation, precipitation, intergranular embrittlement, rapid self-diffusion, and weldability.<sup>[1–4]</sup> Thus, controlling the grain boundary character distribution (GBCD) in microstructures can result in improved functional and mechanical properties. In 1984, Watanabe demonstrated a process termed “grain boundary design and control” to improve the ductility and strength in alpha brass.<sup>[5]</sup> In the 1990s, advancement of electron backscatter diffraction (EBSD) techniques led to further significant investigations in this field, and the process has come to be known as “grain boundary engineering” (GBE). This field has extensively been explored to improve various

grain-boundary-related characteristics of polycrystalline materials, such as intergranular corrosion, stress corrosion cracking, weldability, low- and high-cycle fatigue, high-temperature creep, and electrical conductivity.<sup>[6–9]</sup> GBE modifies the GBCD in a polycrystalline material by increasing the fraction of low- $\Sigma$  coincidence site lattice (CSL) boundaries,  $3 \leq \Sigma \leq 29$ . Here,  $\Sigma$  is the reciprocal fraction of coinciding lattice sites between two adjoining grains, which occur at a certain axis and misorientation angle. These boundaries are commonly known as special boundaries due to their lower energy and consequent better functional properties than random high-angle grain boundaries (HAGBs).<sup>[10]</sup> Among the low- $\Sigma$  CSLs,  $\Sigma 3$ /twins are considered to be the most desirable boundaries, as these boundaries are known to possess the least energy among all the CSL boundaries.<sup>[11,12]</sup> So the GBE concept is generally used in low and medium stacking fault energy (SFE) face-centered-cubic (fcc) materials, which are prone to form annealing twins during recrystallization.<sup>[4,12,13]</sup> Most studies use the Brandon criterion for defining the misorientation range of various CSL boundaries, which allows a deviation of 8.66 deg for the twin boundaries.<sup>[14]</sup> However, experiments show that twin boundaries with large deviations lower the resistance to grain boundary cracking during intergranular degradation.<sup>[12,15–17]</sup> Ortner and Randle<sup>[18]</sup> showed that the precipitates start nucleating at incoherent twin boundaries in sensitized SS304, leading to the formation of Cr-depleted zones at the grain boundaries, resulting in

SANDEEP SAHU, PRABHAT CHAND YADAV, and SHASHANK SHEKHAR are with the Grain Boundary Engineering Lab, Department of Materials Science and Engineering, Indian Institute of Technology Kanpur, Kanpur 208016, India. Contact e-mail: shashank@iitk.ac.in.

Manuscript submitted July 5, 2017.

Article published online December 17, 2017

intergranular stress corrosion cracking in the alloy. Recent works by our group also reported that largely deviated  $\Sigma 3$  boundaries resulted in an increased degree of sensitization in SS304,<sup>[19]</sup> and the actual cut-off deviation for twin boundaries in a recrystallized microstructure is  $\sim 1$  deg,<sup>[20]</sup> a value substantially lower than that defined by the Brandon's criterion. Thus, it is important to have low deviation in  $\Sigma 3$  boundary misorientation for a material to withstand grain-boundary-related degradation. Also, the fraction of  $\Sigma 1$  boundaries should be kept minimum as these boundaries are found to be unstable at elevated temperatures.<sup>[21]</sup>

Though tailoring GBCD is necessary for achieving low-energy microstructure, it is not a sufficient criterion to stop intergranular crack propagation. The network of random boundaries needs to be broken to arrest the crack propagation at the grain boundary junction. Several studies have emphasized the role of connectivity/topology of grain boundaries through triple junction distribution (TJD).<sup>[22,23]</sup> TJD was proposed by Gertsman *et al.*<sup>[24,25]</sup> to classify different types of triple junctions depending upon their ability to arrest intergranular crack propagation. In this classification scheme, each junction is identified as  $J_i$  ( $i = 0$  to  $3$ ) type, where  $i$  represents the number of low- $\Sigma$  CSL boundaries meeting at the triple junction. Here, junctions  $J_2$  and  $J_3$  are considered as special/secure junctions as they predominantly consist of low- $\Sigma$  CSL boundaries and have a high probability of checking intergranular crack propagation to prevent the formation of long crack susceptible paths.<sup>[12,22,25]</sup> Similarly,  $J_0$  and  $J_1$  are described as nonspecial/weak junctions with low probability to arrest the propagation of intergranular cracking. Crack propagation probability could be even higher through these junctions in the presence of external factors such as when the orientation of the applied stress is in the same direction as that of crack extension.<sup>[26]</sup> Thus, for effective GBE of a material, not only the grain boundary character but also the TJD should be assessed. This concept is now commonly known as "triple junction engineering" (TJE).

The GBE process generally comprises a combination of deformation and annealing, typically known as thermomechanical processing (TMP).<sup>[4,12,22,23,27]</sup> In most studies, the GBE process has been applied through multiple cycles of low-level deformation and subsequent annealing steps where intermediate steps tend to increase the fraction of special boundaries in the microstructure.<sup>[28,29]</sup> However, most of these studies, including our own,<sup>[30]</sup> suggest that this kind of process results in a drastic increase in the fraction of thermally unstable  $\Sigma 1$  boundaries; thus, microstructure does not remain stable even at moderately high temperatures.<sup>[21]</sup> Moreover, room-temperature deformation is the commonly applied route in these studies.<sup>[23,28,30,31]</sup> However, the application of multiple cycles of room-temperature deformation followed by annealing is not a commercially feasible process, particularly for producing industrial-scale large, bulky, and complex structures. Also, this kind of process adds to the lead time in the

production line, thereby making the process time-consuming. Some authors have suggested single-step room-temperature deformation and annealing to achieve grain-boundary-engineered microstructure.<sup>[30,32,33]</sup> However, imposing high strains at room temperature in large and bulky industrial structures generates cracks in the materials, sometimes even leading to the failure of the equipment used for applying strain, such as in forging dies.<sup>[34]</sup> Also, it is rather difficult to impart large reduction to high-strength materials, such as nickel-based superalloys and stainless steel, at room temperature without requiring high loads (and, in turn, heavy equipment). To overcome this challenge, some work has also been carried out using low-level strains at room temperature, followed by a long-duration annealing, generally known as strain annealing treatment.<sup>[35-37]</sup> However, long-duration annealing necessitates high power consumption and holding time, thus rendering it unsuitable for industrial applications. Due to these limitations, the GBE process has still not been able to attract much attention from industry as a viable process for improving the physical properties of engineering materials even after 30 years since its first demonstration. The aforementioned limitations may be overcome if the deformation is applied at higher temperature, in a single step, and with short-time postdeformation annealing. High-temperature deformation is also advantageous in lowering the fraction of low-angle grain boundaries (LAGBs)/ $\Sigma 1$ , which, as stated earlier, are unstable at elevated temperatures.

In the present work, we demonstrate a commercially viable process, *i.e.*, hot rolling (high-temperature deformation) followed by a short-time annealing step for achieving GBE of Inconel 600 alloy. Inconel 600 is a standard nickel-based superalloy generally used for high-temperature and anticorrosion applications, such as structural material for nuclear reactors, steam turbines, aircraft engines, high-temperature tooling and dies, and oil and gas equipment.<sup>[38,39]</sup> The GBE treatment can be applied to further improve its properties. This approach leads to an improved GBCD and, hence, improved properties. Additionally, we show that increasing the fraction of special boundaries alone is not sufficient and one needs to look at other parameters, such as topology of the CSL boundaries and their deviation from theoretical misorientation.

## II. MATERIALS AND EXPERIMENTAL PROCEDURE

### A. Materials

Inconel 600 is a high-strength single-phase austenitic nickel-based superalloy with low SFE and fcc crystal structure; hence, it is suitable for studying the effectiveness of hot rolling in modifying the GBCD and network topology. A rectangular plate of Inconel 600 alloy was purchased from Amco Metals (Mumbai, India). The chemical composition of the alloy (Table I) was confirmed using optical emission spectroscopy (OES).

**Table I. Chemical Composition of Inconel 600 Alloy as Measured Using OES**

Element	Cr	Fe	Ti	C	Mn	S	Si	Cu	Ni
Composition (Wt Pct)	16.5	7.38	0.22	0.059	0.18	< 0.001	0.28	0.051	balance

### B. Thermomechanical Processing

Six rectangular strips of dimensions 50 mm × 15 mm × 6.1 mm were cut from an Inconel 600 plate. These strips were annealed at 1373 K (1100 °C) for 2 hours to homogenize their microstructure. Subsequently, the annealed samples were water quenched to retain the high-temperature microstructure at room temperature and also to avoid sensitization.<sup>[40]</sup> This sample condition has been termed the “as-received” sample, designated as A0. Six strips of the as-received sample, A0, were hot rolled at 1273 K (1000 °C) using a double mill rolling machine (loading capacity: 100 ton, roll diameter: 200 mm, and rolling speed: 35 rpm), leading to thickness reductions of 4, 8, 11, 15, 19, and 22 pct, respectively, in a single step, followed by water quenching. The corresponding true strains were ~ 4, 8, 12, 16, 20, and 25 pct, respectively, and the samples are designated as R1, R2, R3, R4, R5, and R6, respectively. A small piece of size 20 mm × 10 mm was cut from each of these rolled strips and was subjected to a short-duration heat treatment at 1273 K (1000 °C) for 10 minutes, followed by water quenching. Short-time annealing was selected to avoid any excessive grain growth.<sup>[41]</sup> These samples have been referred to as annealed/heat-treated samples, designated as A1, A2, A3, A4, A5, and A6, corresponding to their rolled counterparts.

### C. Grain Boundary and Triple Junction Characterization

For microstructural characterization, small test coupons from the processed samples were initially cut and then sectioned at the midthickness region using a low-speed diamond cutter with liberal use of lubricant, also serving as a coolant to avoid the shearing effect of rolling and any other artifacts associated with the sample’s surface that might interfere with the analysis.<sup>[27,42]</sup> Figure 1 shows a schematic of the plane used for the characterization of thermomechanically processed samples. The rolling direction–transverse direction (RD–TD) plane of these samples was mechanically polished in a sequence using SiC papers of grit sizes 180 to 2000 followed by cloth polishing using diamond paste of size 1 μm, to obtain a mirrorlike surface. The samples were then electropolished using Struers Lectropol 5 in Struers standard A2 electrolyte at 30 V, 248 K (– 25 °C) for 25 seconds to obtain a strain-free sample surface suitable for EBSD analysis. OIM maps were obtained in the electropolished region using an Oxford Instruments Nordlys EBSD detector attached to a JEOL JSM-7100F field-emission scanning electron microscope. EBSD patterns were acquired under the following conditions: accelerating voltage 20 keV, electron beam probe current ~ 12 nA, and working distance ~ 17 mm with the

sample holder’s position tilted by 70 deg to the primary electron beam direction. The EBSD camera binning used was 4 × 4, the step size was 1 μm, and the Kikuchi patterns were indexed for the Ni superalloy phase, predefined in the HKL database. The mean angular deviation was used as a statistical measure of accuracy during Kikuchi pattern indexing. The indexing rate was more than 96 pct in all the OIM maps. Multiple areas of size ranging from 2 × 10<sup>5</sup> to 2 × 10<sup>6</sup> μm<sup>2</sup> were scanned during EBSD data acquisition, and a minimum of five maps were acquired for each sample condition to ensure statistically significant results. The EBSD scans were taken at random places (but close to the geometric center plane of the sample) to cover significantly different kinds of regions. The acquired OIM maps were analyzed using HKL channel 5 (Oxford Instruments) and TSL OIM, version 7.3 (energy-dispersive X-ray analysis) software. It is known that for a certain SFE of a material, a relative equilibrium state of the grain boundaries is achieved by increasing the total length of low-energy CSL boundaries, instead of the number of these boundaries. So, we measured the length fraction of these grain boundaries using HKL channel 5 Tango software to categorize the length fraction of various kinds of boundaries, such as LAGBs, CSL boundaries, and random HAGBs. The length fraction of any particular CSL boundary was calculated by dividing the total length of that CSL boundary by the total length of all the boundaries present in the microstructure. The length of a boundary was equal to the number of pixels belonging to that particular boundary multiplied by the step size. Since the angular resolution of EBSD is of the order of 1 deg,<sup>[43,44]</sup> the grains were defined for a minimum misorientation of 2 deg. LAGBs/Σ1 have been defined for a misorientation angle in the range of 2 to 15 deg and HAGBs for a misorientation angle ≥ 15 deg and Σ > 29. The total low-Σ CSL boundaries have been defined for 3 ≤ Σ ≤ 29, allowing the deviation per the commonly used Brandon criterion,<sup>[14]</sup> given as  $\Delta\theta = \theta_m/\Sigma^{1/2}$ , where  $\Delta\theta$  is the maximum deviation angle allowed from the exact/theoretical CSL misorientation and  $\theta_m$  denotes the maximum misorientation angle for a LAGB (typically taken as 15 deg). The Brandon criterion was used to compare our results with the other literature data. However, we also performed a deviation-based analysis of twin boundaries in order to ascertain the fraction of “effective twin boundaries,” which show better properties. For the grain size analysis, a grain was defined for a misorientation greater than 10 deg and containing a minimum of 4 pixels (equivalent to an area of 4 μm<sup>2</sup>). The triple junction analysis was performed by TSL OIM software, version 7.3 in order to evaluate the grain boundary network topology. The fraction of all types of grain boundaries and triple junctions was obtained by

averaging the EBSD results of different regions, and the values are reported here along with the standard error.

### III. RESULTS

#### A. Grain Boundary Character of As-Received Sample

An OIM analyzed inverse pole figure (IPF) map of the as-received sample, A0, is shown in Figure 2(a), where a standard stereographic triangle corresponds to various crystallographic directions indicated by different colors and, evidently, the grains are oriented in different directions. Figure 2(b) presents a band contrast map overlaid with various kinds of grain boundaries. Here,  $\Sigma 1$ ,  $\Sigma 3$ ,  $\Sigma 9$ , and  $\Sigma 27$  and random HAGBs are shown by green, red, blue, aqua, and black lines, respectively. It can be seen that the grains are nearly equiaxed, albeit with a large variation in grain sizes. Also, it can be observed that both the large and small size grains contain straight and parallel-sided  $\Sigma 3$  boundaries, which indicate that twins were generated during the recrystallization as well as the grain growth stage during homogenization treatment. As shown in Figure 2(c), the  $\{111\}$  pole figure calculated for  $\sim 925$  grains suggests the absence of strong texture in the initial microstructure. The estimated grain sizes were  $60 \mu\text{m}$  [inclusive of twins (IT)] and  $100 \mu\text{m}$  [exclusive of twins (ET)]. A statistical analysis of the grain boundary length revealed that the fraction of low- $\Sigma$  CSL boundaries was 60.3 pct, with a distribution of 55.1 pct  $\Sigma 3$  and 5.2 pct other special boundaries. The low-angle boundary or  $\Sigma 1$  length fraction was 2.5 pct, while that of the random HAGBs was 47.2 pct. Figure 2(d) depicts the grain boundary misorientation angle distribution of the as-received sample, A0, which shows that most of the twins are present in the vicinity of 60 deg misorientation and, hence, are likely to be coherent. During the process of  $\Sigma 3$  regeneration,  $\Sigma 9$  and  $\Sigma 27$  boundaries are considered as the geometrical necessity that plays a major role in breaking the random grain boundary networks. The as-received sample, A0, had a very low fraction of  $\Sigma 9$  and  $\Sigma 27$  boundaries (Table II). The occurrence of intragranular twin boundaries and low fraction of  $\Sigma 9$  and  $\Sigma 27$  boundaries indicates the presence of interconnected random grain boundary networks throughout the microstructure, as can be observed in Figure 2(b). Earlier works have shown that this kind of network leads to failure during high-temperature applications and intergranular corrosion attack where cracks

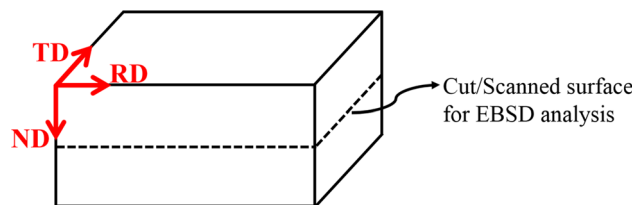


Fig. 1—Schematic for hot rolling directions (RD, TD, and ND: normal direction), where the dashed line corresponds to the section used for EBSD analysis.

propagate through the well-connected random boundary network to propagate in the entire sample.<sup>[22,25]</sup> Therefore, the fraction of special boundaries needs to be increased and the connectivity of random boundaries needs to be disrupted (through an economical, easy, and industrially feasible route), which can improve the intergranular resistance of Inconel 600 alloy.

#### B. Effect of Processing on GBCD

Table II gives detailed information about the different kinds of grain boundaries observed for various sample conditions. This table shows the length fraction of  $\Sigma 1$ ,  $\Sigma 3^n$  ( $n = 1$  to 3), and total low- $\Sigma$  CSL ( $3 \leq \Sigma \leq 29$ ) boundaries along with grain size for all the sample conditions. The grain size was calculated in two different ways: by considering the twins as boundaries during grain size calculation, called IT grain size, and by excluding the twins during grain size calculation, called ET grain size. This was done to calculate the twin density in various sample conditions. Figures 3 and 4 present the representative OIM band contrast maps overlaid with various kinds of grain boundaries for the rolled samples, R1 through R6, and their annealed counterparts, A1 through A6, respectively, showing microstructural evolution as a result of different processing conditions. Here, LAGBs  $\Sigma 1$ ,  $\Sigma 3$ ,  $\Sigma 9$ , and  $\Sigma 27$  and random HAGBs are shown in green, red, blue, aqua, and black lines, respectively. These maps show a qualitative distribution of various kinds of grain boundaries, while the quantitative variation in the length fraction of  $\Sigma 1$ ,  $\Sigma 3$ , and total low- $\Sigma$  CSL ( $3 \leq \Sigma \leq 29$ ) boundaries with the increase in rolling strain and subsequent annealing treatment is shown in Figure 5. It is clearly seen in Figure 3 that there are not many elongated structures in the rolled samples, which is probably due to the dynamic recrystallization taking place in these samples.<sup>[45]</sup> However, the effect of rolling is reflected in terms of the generation of more and more dislocations with the increase in the rolling strain. Also, with 12 pct and higher strain, a few inhomogeneous grains can be observed. This can be the effect of rolling, during which grains having certain orientations with respect to the RD experience comparatively higher strain than the other grains, and this effect increases with the increase in the rolling strain.<sup>[26]</sup> Compared to R1 through R6, the sample conditions A1 through A6 have more red lines, indicating a high fraction of  $\Sigma 3$  boundaries, and almost negligible green lines, corresponding to a very low fraction of LAGBs. A typical grain boundary misorientation angle distribution for the processed samples A1 through A6 is also shown in Figure 6. These misorientation angle plots provide an in-depth understanding of the rearrangement and development of various kinds of grain boundaries occurring during TMP.

When we consider GBE, we should keep in mind that the length fraction of various boundaries in itself is not sufficient to predict the amount of cracking during an intergranular corrosion attack as the size of the grains also influences cracking. On one hand, a sample with a smaller grain size can be expected to show more

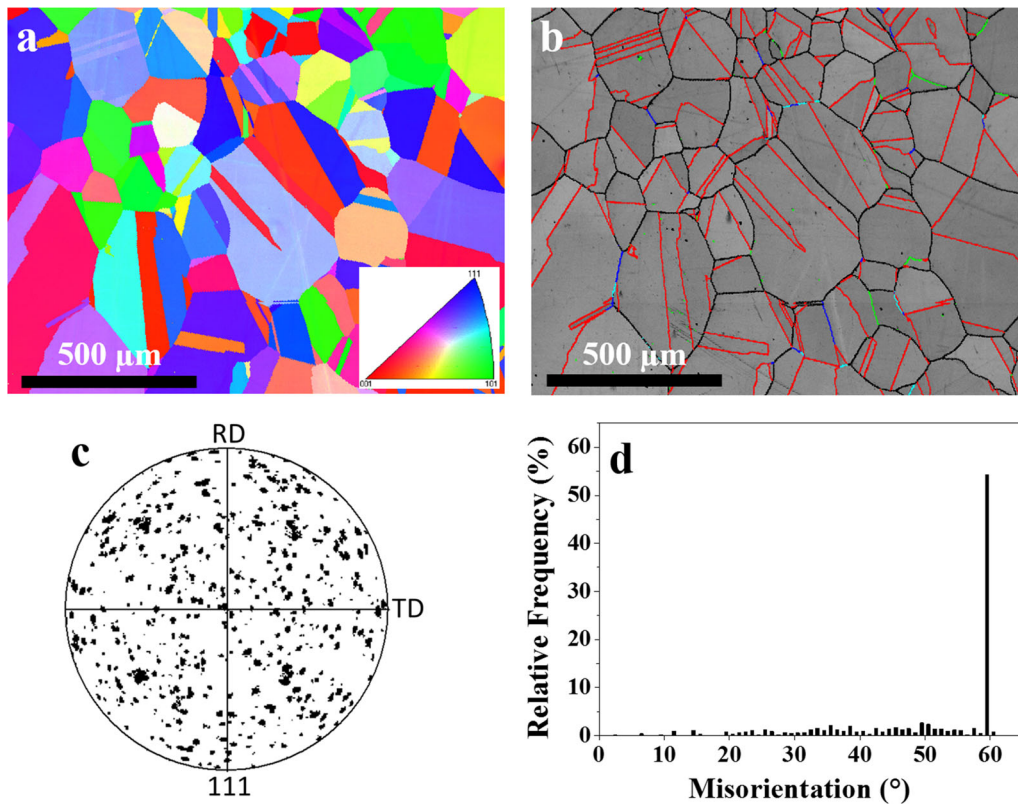


Fig. 2—(a) IPF map, (b) OIM band contrast map overlaid with various kinds of grain boundaries (green:  $\Sigma 1$ , red:  $\Sigma 3$ , blue:  $\Sigma 9$ , aqua:  $\Sigma 27$ , and black: random HAGBs), (c)  $\{111\}$  pole figure, and (d) grain boundary misorientation angle distribution in the starting (*i.e.*, as-received) Inconel 600 alloy, A0 (Color figure online).

**Table II. CSL Fraction and Grain Size for the Samples Processed Through Hot Rolling and Subsequent Short-Time Annealing**

Sample Condition	$\Sigma 1$ (Pct)	$\Sigma 3$ (Pct)	$\Sigma 9$ (Pct)	$\Sigma 27$ (Pct)	Total Low- $\Sigma$ CSL ( $3 \leq \Sigma \leq 29$ ) (Pct)	Grain Size (IT) ( $\mu\text{m}$ )	Grain Size (ET) ( $\mu\text{m}$ )
A0	$2.5 \pm 0.5$	$55.1 \pm 0.6$	$1.6 \pm 0.5$	$0.5 \pm 0.0$	$60.3 \pm 0.5$	$59.9 \pm 4.5$	$99.2 \pm 3.8$
R1	$5.4 \pm 1.5$	$51.0 \pm 1.8$	$3.2 \pm 0.2$	$0.7 \pm 0.1$	$57.6 \pm 0.2$	$20.7 \pm 2.3$	$47.7 \pm 4.9$
R2	$10.5 \pm 0.3$	$57.1 \pm 0.4$	$3.9 \pm 0.2$	$0.7 \pm 0.0$	$63.2 \pm 0.5$	$13.1 \pm 0.5$	$39.4 \pm 3.3$
R3	$44.2 \pm 1.6$	$28.4 \pm 0.8$	$1.2 \pm 0.1$	$0.2 \pm 0.0$	$31.1 \pm 0.9$	$13.8 \pm 0.8$	$30.1 \pm 1.9$
R4	$51.4 \pm 0.8$	$24.4 \pm 1.0$	$0.9 \pm 0.1$	$0.2 \pm 0.0$	$26.7 \pm 1.1$	$12.6 \pm 0.3$	$23.3 \pm 0.4$
R5	$57.2 \pm 0.7$	$16.6 \pm 0.5$	$0.4 \pm 0.0$	$0.1 \pm 0.0$	$18.6 \pm 0.5$	$16.5 \pm 0.9$	$23.2 \pm 0.9$
R6	$75.2 \pm 1.0$	$7.1 \pm 0.5$	$0.2 \pm 0.0$	$0.0 \pm 0.0$	$8.4 \pm 0.5$	$12.0 \pm 1.2$	$12.0 \pm 0.8$
A1	$4.0 \pm 0.3$	$58.0 \pm 1.4$	$4.3 \pm 0.4$	$1.2 \pm 0.2$	$65.6 \pm 1.5$	$14.5 \pm 0.9$	$38.6 \pm 0.3$
A2	$8.0 \pm 1.8$	$55.7 \pm 1.9$	$3.9 \pm 0.7$	$1.4 \pm 0.5$	$63.0 \pm 3.0$	$14.0 \pm 0.3$	$35.9 \pm 2.9$
A3	$1.4 \pm 0.1$	$64.2 \pm 1.1$	$7.1 \pm 0.2$	$4.2 \pm 0.1$	$76.9 \pm 1.2$	$12.9 \pm 0.5$	$38.0 \pm 0.9$
A4	$1.5 \pm 0.1$	$60.2 \pm 1.1$	$6.8 \pm 0.3$	$3.9 \pm 0.2$	$72.6 \pm 1.2$	$11.9 \pm 0.3$	$34.2 \pm 1.1$
A5	$2.1 \pm 0.3$	$56.4 \pm 1.5$	$3.8 \pm 0.2$	$1.9 \pm 0.3$	$64.3 \pm 1.6$	$18.0 \pm 1.4$	$44.7 \pm 3.1$
A6	$1.6 \pm 0.1$	$57.5 \pm 1.0$	$5.3 \pm 0.2$	$2.7 \pm 0.1$	$67.7 \pm 0.8$	$9.9 \pm 0.3$	$26.7 \pm 1.1$

degradation on the surface (during an intergranular cracking) because of the larger length as well as due to the higher number of regular grain boundaries per unit area. However, on the other hand, smaller grains have shorter length of regular boundaries per grain; therefore, the probability of them getting disrupted (with the incorporation of CSL boundaries) is higher. This, in turn, would decrease the average depth of penetration during intergranular degradation. The ET grain size distribution in the as-received sample, A0, and the

thermomechanically processed samples, A1 through A6, is presented in Figure 7. It is seen that all the heat-treated samples, A1 through A6, show peaks at smaller grain size values, while the as-received sample, A0, shows several small peaks at relatively larger grain size values. Thus, the as-received sample, A0, consists of significantly large size grains in comparison to those in the processed samples; hence, the depth of intergranular degradation can be expected to be smaller for the processed samples, A1 through A6, in comparison to

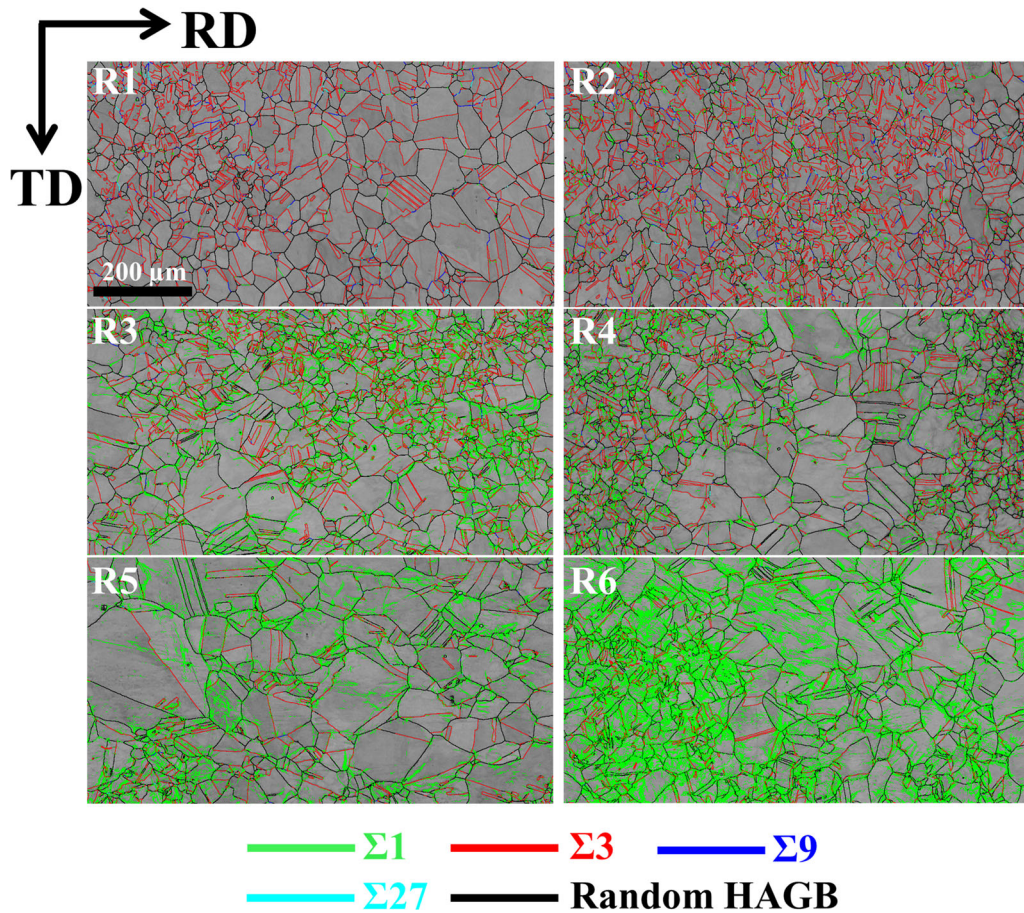


Fig. 3—OIM band contrast map overlaid with different kinds of grain boundaries (LAGBs,  $\Sigma_3$ ,  $\Sigma_9$ ,  $\Sigma_{27}$ , and random HAGBs) for various as-rolled samples (scale bar for R1 applies to all the OIM maps) (Color figure online).

that of A0, provided the connectivity of random grain boundaries is sufficiently disrupted.<sup>[12,22]</sup>

#### IV. DISCUSSION

##### A. Effect of Strain and Annealing on GBCD

###### 1. Effect of strain

The strain and rolling conditions used in this work should lead to dynamic recrystallization of all the rolled sample conditions (R1 through R6), as suggested by Wu *et al.*<sup>[45]</sup> Moreover, the strain softening should dominate for R1 and R2 conditions, while strain hardening should dominate for R3 through R6 sample conditions. As shown in Figure 5(a), strain softening during dynamic recrystallization leads to a very small increase in  $\Sigma_1$  boundaries (in R1 and R2), while a very large increase in  $\Sigma_1$  boundaries can be observed for higher strained samples (R3 through R6). Such a large increase in  $\Sigma_1$  boundaries for R3 through R6 can be attributed to the generation of more and more dislocations, which eventually form cell walls and cell boundaries. The fraction of  $\Sigma_3$  boundaries does not change much for R1 and R2, which can again be related to the strain softening in these samples, while for R3 and higher strained samples, the length fraction of  $\Sigma_3$

boundaries decreases continuously up to R6. The length fractions of  $\Sigma_1$  and  $\Sigma_3$  were found to be the inverse of each other, which can be understood from the fact that, as more and more dislocations are generated, they disrupt  $\Sigma_3$  boundaries, thus reducing their fraction. Concomitantly, these dislocations collate together, increasing the fraction of  $\Sigma_1$  boundaries. So, the higher the number of dislocations, the higher is the probability of  $\Sigma_3$  becoming disrupted and broken. As mentioned previously, only R3 and higher strained samples showed drastic change in the fraction of  $\Sigma_1$  and  $\Sigma_3$  boundaries. Since strain hardening dominates in these samples, it can be argued that the strain in these samples is sufficiently large and is uniformly distributed in the microstructure; concomitantly, twin boundaries become broken homogeneously across the sample. The grain size of all the rolled samples, R1 through R6, shows a substantial reduction in comparison to that of the as-received sample, A0 (Table II). This reduction in grain size is also directly related to the dynamic recrystallization that is known to occur at these conditions for Inconel 600 alloy.<sup>[45]</sup>

###### 2. Effect of annealing

Figure 5(b) shows the length fraction of various boundaries after the annealing of rolled samples. It

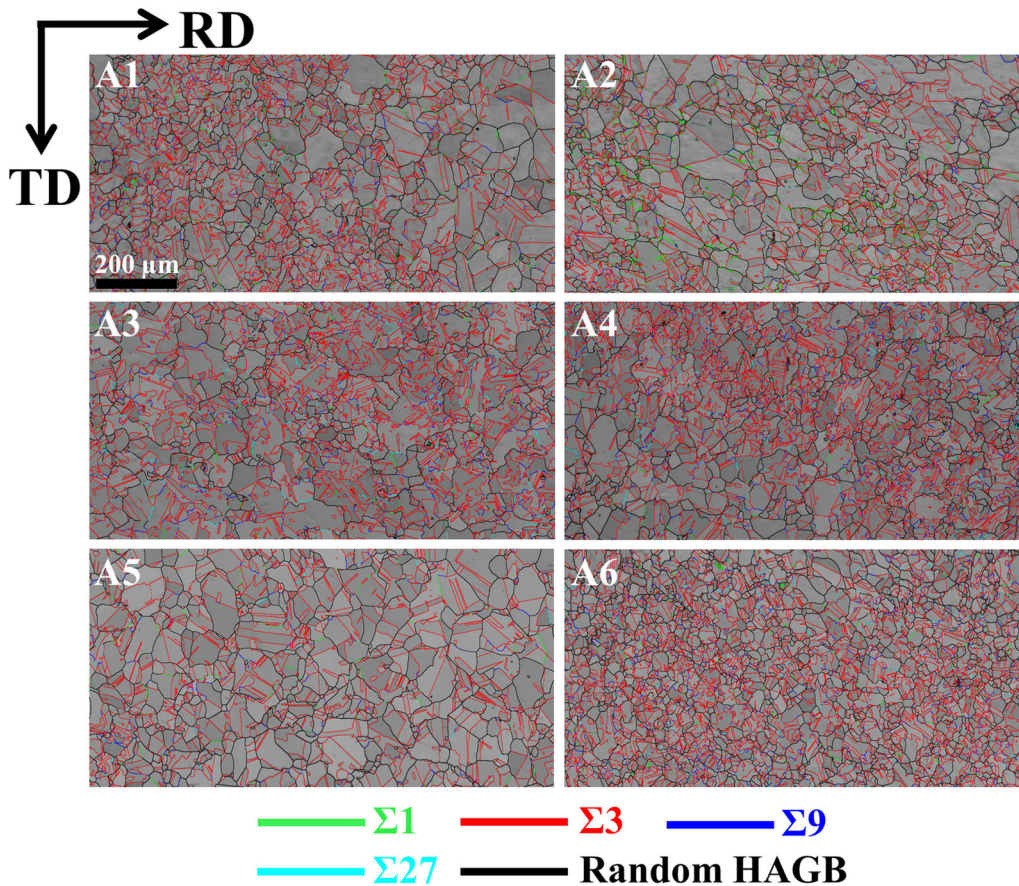


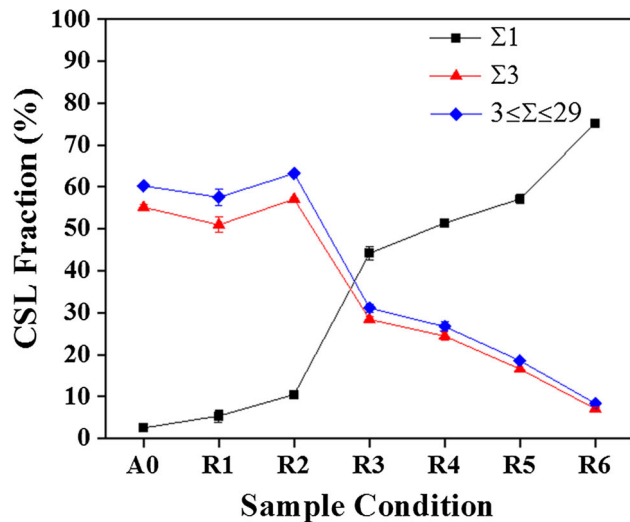
Fig. 4—OIM band contrast map overlaid with different kinds of grain boundaries (LAGBs,  $\Sigma 3$ ,  $\Sigma 9$ ,  $\Sigma 27$ , and random HAGBs) for various annealed samples (scale bar for A1 applies to all the OIM maps) (Color figure online).

can be seen that the heat treatment of R1 and R2 sample conditions (*i.e.*, A1 and A2) does not lead to much variation in either  $\Sigma 1$  or  $\Sigma 3$  length fraction, in comparison to that of the rolled conditions, R1 and R2, respectively. This negligible change can be ascribed to the strain softening during hot rolling, leading to the recovery of strain generated during rolling steps R1 and R2; as a result, the samples do not have enough driving force to induce recrystallization during the short heat treatment of 10 minutes. However, as a caution, it must be noted that, even though the total low- $\Sigma$  CSL fraction remains almost constant, twin characteristics do vary between A1 and A2 sample conditions. Since strain hardening dominates in R3 through R6 sample conditions, there is enough driving force to cause static recrystallization during the short heat treatment of 10 minutes (*i.e.*, for A3 through A6).

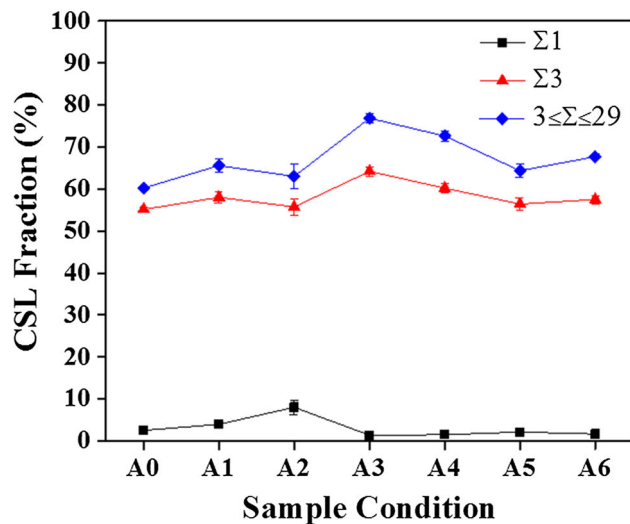
Although A3 through A6 samples underwent static recrystallization, no improvement in their grain boundary characteristics was observed. The fraction of low- $\Sigma$  CSL ( $3 \leq \Sigma \leq 29$ ) boundaries is significantly lower for A4, A5, and A6 sample conditions compared to that of A3. It is also observed that A3 has a comparatively higher contribution from other variants of  $\Sigma 3$  boundaries (*i.e.*,  $\Sigma 9$  and  $\Sigma 27$ ) than those in the other sample conditions (as seen from Table II), which are generally less reactive than the other boundaries in  $5 \leq \Sigma \leq 29$ . As

a consequence of the high fraction of low- $\Sigma$  CSL boundaries, the A3 sample also results in the lowest random HAGB fraction. Since random HAGBs are the most active boundaries during an intergranular reaction, having the lowest fraction of these boundaries in the A3 sample suggests it to be least reactive during any grain-boundary-related degradation. These results suggest that, to obtain desirable GBCD, deformation should be sufficiently high to cause postprocess static recrystallization but also low enough to minimize the breaking of the original CSL boundaries and their networks. We do not obtain desirable GBCD during dynamic recrystallization; hence, static recrystallization is necessary for improving GBCD. The role of postdeformation annealing is to ensure that recrystallization takes place, which is necessary not only for increasing the fraction of low- $\Sigma$  CSL boundaries but also for improving the fraction of low deviation CSL boundaries.

Static recrystallization during postdeformation annealing can also be understood using the misorientation plot shown in Figure 6 for A1 through A6 sample conditions. Here, we can clearly see that A1 and A2 samples have a broad peak around 60 deg along with a few narrow peaks at low misorientation angle ( $< 15$  deg), suggesting that only recovery (and not recrystallization) takes place in these sample conditions.



(a)



(b)

Fig. 5—Variation in length fraction of LAGBs ( $\Sigma 1$ ), twin boundaries ( $\Sigma 3$ ), and total low- $\Sigma$  CSL boundaries ( $3 \leq \Sigma \leq 29$ ) for (a) rolled and (b) annealed samples.

The misorientation plots for A3 through A6 sample conditions are typical of recrystallized conditions with a comparatively large fraction of  $\Sigma 9$  and  $\Sigma 27$ , large and narrow peaks for  $\Sigma 3$ , and almost no peaks for LAGBs. Evidently, among all the sample conditions, A3 has the highest peak near 60 deg misorientation, representing the maximum  $\Sigma 3$  length fraction among all the processed samples. Also, although the A0 sample condition has undergone recrystallization, it does not show the similar kind of CSL fraction as observed in A3 and in the other processed samples. This clearly emphasizes the need for a properly designed TMP protocol to implement effective GBE.

Further, to have a better understanding of the effect of annealing on deformed samples in the generation of  $\Sigma 3$  boundaries at the cost of  $\Sigma 1$  and random boundaries,  $\Delta(\Sigma 1)$  and  $\Delta(\Sigma 3)$  were plotted for all the sample conditions (Figure 8). Here,  $\Delta(\Sigma 1)$  and  $\Delta(\Sigma 3)$  denote the change in  $\Sigma 1$  and  $\Sigma 3$  length fractions between an

annealed and its respective deformed sample condition for a particular strain. The plot shows that there is always an increase in  $\Sigma 3$  and a corresponding reduction in  $\Sigma 1$  length fraction during subsequent annealing of the deformed samples, beyond strains produced in the R2 sample condition. A3-R3 shows a sharp jump in  $\Delta(\Sigma 3)$  and  $\Delta(\Sigma 1)$  values, which remains almost invariant beyond this sample condition. This rolling step clearly highlights the role of deformation in initiating recrystallization during annealing. A lower strain during R1 and R2 is not sufficient to provide the driving force to initiate recrystallization during the subsequent short heat treatment of 10 minutes. It happens only during R3 and higher strain conditions. This critical strain (12 pct) leads to an appropriate driving force for the generation of low- $\Sigma$  CSL boundaries during the short-time annealing through grain boundary migration and recrystallization.<sup>[4]</sup> Annealing treatment triggers the boundaries to move or migrate toward a specific misorientation (e.g., 60 deg/ $\langle 111 \rangle$  for  $\Sigma 3$ ) to minimize the stored internal energy, which can be inferred through the formation of  $\Sigma 3''$  boundaries,<sup>[4,46]</sup> and recrystallization causes the formation of new annealing twins. A strain below this level is unable to cause recrystallization, while beyond A3, *i.e.*, during A4, A5, and A6, the grain boundary transformation reaches saturation; hence, there is no substantial gain in  $\Sigma 3$  length fraction. From this analysis, it is again clear that R3 (*i.e.*, 12 pct strain) is the most appropriate deformation for obtaining an improved GBCD. However, it needs to be emphasized that the value of 12 pct strain is valid only for the deformation applied at a particular temperature (1273 K (1000 °C) in the present case) and, naturally, it will vary with processing conditions. At ambient or any other environmental temperature, the critical strain may be different and will have to be evaluated.

The effectiveness of GBE can also be measured in terms of the average number of twin boundaries per grain; hence, this parameter was calculated to ascertain the efficacy of various sample conditions. This objective is accomplished here by taking the ratio of grain size obtained in two different ways, *viz.* ET grain size and IT grain size, as suggested by Field *et al.*<sup>[47]</sup> Effective twin density (*i.e.*, average number of twin boundaries per grain) for all the sample conditions is shown in Figure 9. Although TMP can be seen to increase the twin density for all sample conditions, the average number of twins per grain is the highest for A3, followed by that for A4, and it is substantially lower for the other conditions (*i.e.*, A1, A2, A5, and A6). This further emphasizes that only 12 and 16 pct true strain can be expected to produce an effective GBE during annealing, and it is not useful to go beyond these strains at a particular deformation temperature.

### B. Mechanism of Twin Evolution

It is known that GBE is realized through proliferation of  $\Sigma 3$  boundaries in low SFE materials. However, as discussed earlier,  $\Sigma 9$  and  $\Sigma 27$  boundaries can be construed as geometrically necessary boundaries during the interaction of various  $\Sigma 3$  boundaries; hence,



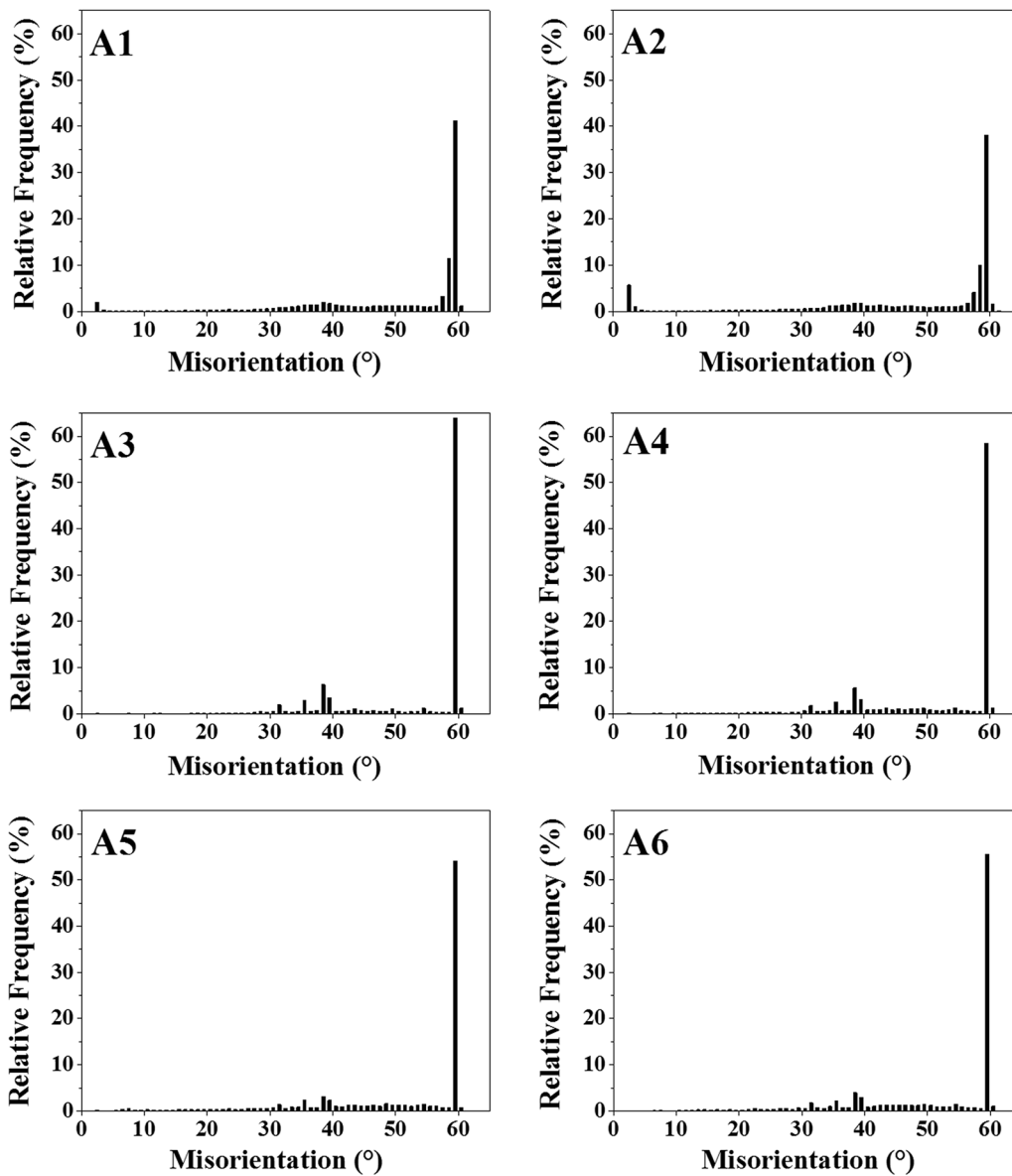


Fig. 6—Grain boundary misorientation angle distribution in various sample conditions.

evolution of  $\Sigma 9$  and  $\Sigma 27$  boundaries can also be used to predict the extent of GBE as well as the proliferation of  $\Sigma 3$  boundaries. A large fraction of  $\Sigma 3^n$  ( $n = 1$  through 3) boundaries and their mutual interactions can help in disrupting the random HAGB network. The variation in the length fractions of  $\Sigma 9$  and  $\Sigma 27$  with various sample conditions, as shown in Figure 10, follows a trend similar to that of  $\Sigma 3$  and total low- $\Sigma$  CSL fraction (shown in Figure 5). However, except A3 and A4, for the other sample conditions, the corresponding jump/drop of  $\Sigma 9$  and  $\Sigma 27$  is not in the same proportion as that for  $\Sigma 3$ . There is a sharp rise in  $\Sigma 9$  and  $\Sigma 27$  boundary length fractions for A3 and A4 sample conditions, similar to that for  $\Sigma 3$  and total low- $\Sigma$  CSL fraction. The presence of large fractions of  $\Sigma 9$  and  $\Sigma 27$  boundaries indicates that the  $\Sigma 3^n$  regeneration/multiple twinning mechanism is dominant for A3 and A4 sample conditions. According to the “ $\Sigma 3$  regeneration model,”

proposed by Randle, two  $\Sigma 3^n$  boundaries conjoin to produce another  $\Sigma 3^n$  boundary.<sup>[2]</sup> The grain boundaries intersecting at a junction can be identified using the addition rule, particularly for CSL boundaries.<sup>[2,48]</sup> The addition rule can be expressed as  $\Sigma A + \Sigma B \Rightarrow \Sigma(A \times B)$  or  $\Sigma(A/B)$ . A relatively high proportion of  $\Sigma 9$  and  $\Sigma 27$  boundaries in such materials are due to geometrical constraints only and, as such, are not related to the energy of individual grain boundaries. These are necessary for providing connections between  $\Sigma 3$  boundaries in the process of multiple twinning and development of a grain boundary network. The high fractions of  $\Sigma 9$  and  $\Sigma 27$  boundaries in the A3 sample condition can also be inferred from its misorientation angle distribution plot shown in Figure 6(A3), which depicts the peaks at 38.94 deg ( $\Sigma 9$ ), 31.58 deg ( $\Sigma 27a$ ), and 35.42 deg ( $\Sigma 27b$ ). A low fraction of  $\Sigma 9$  and  $\Sigma 27$  usually indicates that the  $\Sigma 3^n$  regeneration mechanism

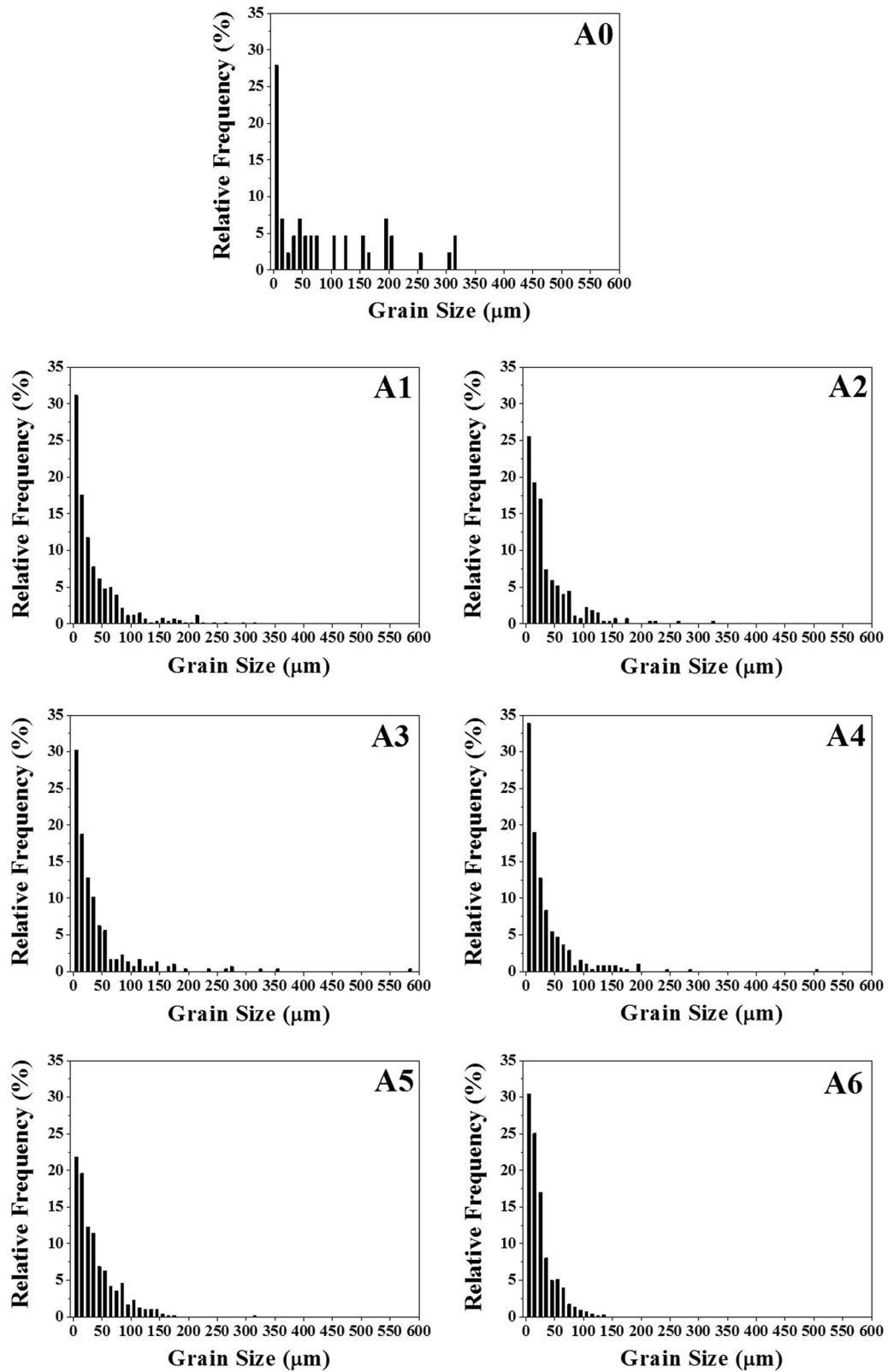


Fig. 7—Grain size distribution in various sample conditions.

contributes little. In such cases, it is likely that  $\Sigma 3$  boundaries are generated through a new twin formation mechanism.

A better parameter to properly identify the mode of twin growth is  $\Sigma 3 / (\Sigma 9 + \Sigma 27)$ .<sup>[12,49,50]</sup> It has been reported that a lower value of  $\Sigma 3 / (\Sigma 9 + \Sigma 27)$  is related

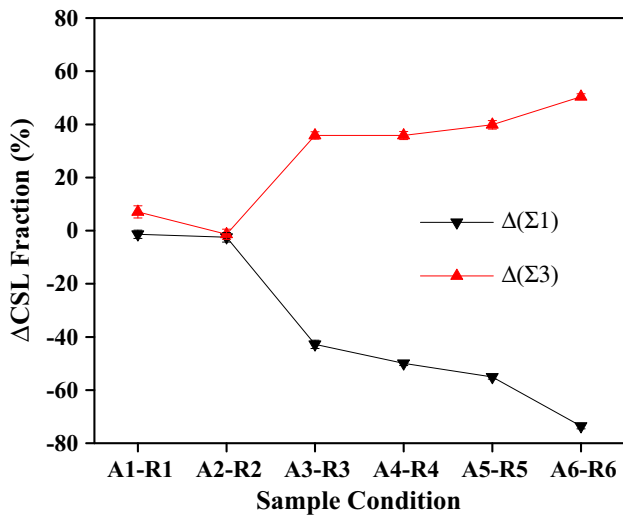


Fig. 8—Variation of  $\Delta(\Sigma 1)$  and  $\Delta(\Sigma 3)$  with increasing strain.

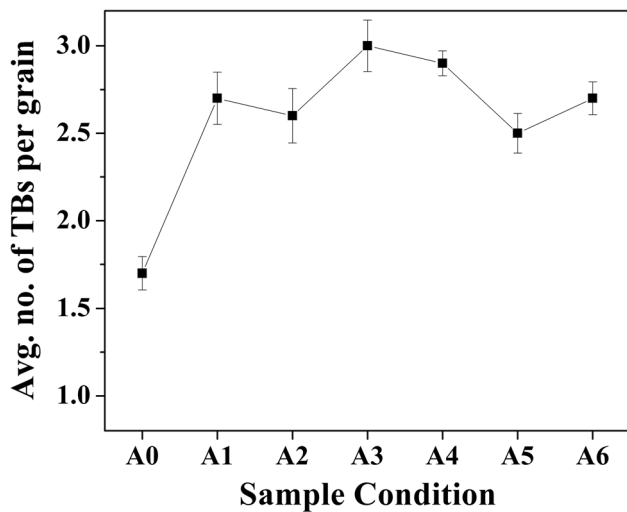


Fig. 9—Variation in average number of twin boundaries per grain for various sample conditions.

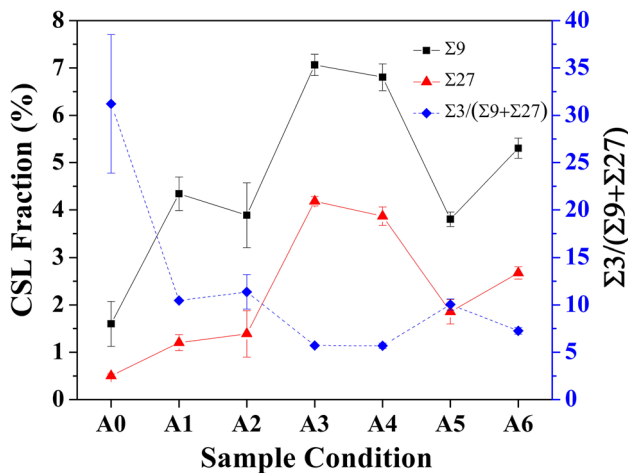


Fig. 10—Variation in  $\Sigma 9$ ,  $\Sigma 27$ , and  $\Sigma 3/(\Sigma 9 + \Sigma 27)$  for various sample conditions.

to the  $\Sigma 3^n$  regeneration mechanism (due to higher mutual interactions of  $\Sigma 3^n$  grain boundaries) during the microstructural evolution, while a higher value represents the new twin formation mechanism.<sup>[12,49,50]</sup> This factor has been used in the literature to understand the twinning mechanism during GBE studies.<sup>[51,52]</sup> The values of this factor for various sample conditions are shown in Figure 10. Clearly, A3 and A4 sample conditions have very low values of  $\Sigma 3/(\Sigma 9 + \Sigma 27)$ , which further confirms that  $\Sigma 3^n$  regeneration is the dominant mechanism for A3 and A4 sample conditions. A0 shows a very high value of  $\Sigma 3/(\Sigma 9 + \Sigma 27)$ , which implies that most of the  $\Sigma 3$  boundaries in the as-received sample were generated by a new twin formation mechanism. For sample conditions A1, A2, A5, and A6, the  $\Sigma 3^n$  regeneration mechanism is not very pronounced and it is likely that a significant fraction of  $\Sigma 3$  boundaries is generated by a new twin formation mechanism. We illustrate various subsets of the A3 sample showing various  $\Sigma 3^n$  interactions generated due to the  $\Sigma 3^n$  regeneration mechanism at several triple junctions in Figure 11. These types of interactions can be observed to increase the number fraction of  $\Sigma 9$  and  $\Sigma 27$  boundaries.

The value of  $\Sigma 3/(\Sigma 9 + \Sigma 27)$  can also be used to understand the proliferation of these boundaries and its ability to disrupt the connectivity of random HAGBs.<sup>[49–51]</sup> Twins formed by the new twinning mechanism do not necessarily form part of the grain boundary network, while those produced through the  $\Sigma 3^n$  regeneration mechanism are directly incorporated into the random boundary network. In the present case, the lowest value of  $\Sigma 3/(\Sigma 9 + \Sigma 27)$  for A3 and A4 sample conditions can be expected to result in the most disrupted random HAGB network, while the as-received sample, A0, can be expected to possess the most connected random HAGB network among all the sample conditions. These results further corroborate our earlier assertion that 12 and 16 pct true stain are the critical deformation conditions that help in achieving a disconnected random boundary network during subsequent annealing.

### C. Deviation from Theoretical Misorientation

Another important factor besides the increment in  $\Sigma 3$  and other CSL boundaries is the character of these boundaries. Deviation from the exact theoretical misorientation is one of the important parameters to quantify the character of these boundaries, which, in turn, determines the properties exhibited by the material.<sup>[20]</sup> A smaller deviation from the exact misorientation can be expected to provide better mechanical and functional response, e.g., corrosion resistance.<sup>[17,19,53]</sup> Since  $\Sigma 3$  boundaries are the dominant fraction and the properties of a material depend mainly on the structure of  $\Sigma 3$  boundaries, allowing a liberal deviation per the Brandon criterion might not be the correct representative of the GBCD of a material. At large deviation, twin characteristics change and it may no longer exhibit special properties. Thus, assessment of the  $\Sigma 3$  deviation from exact misorientation could indicate the true character of

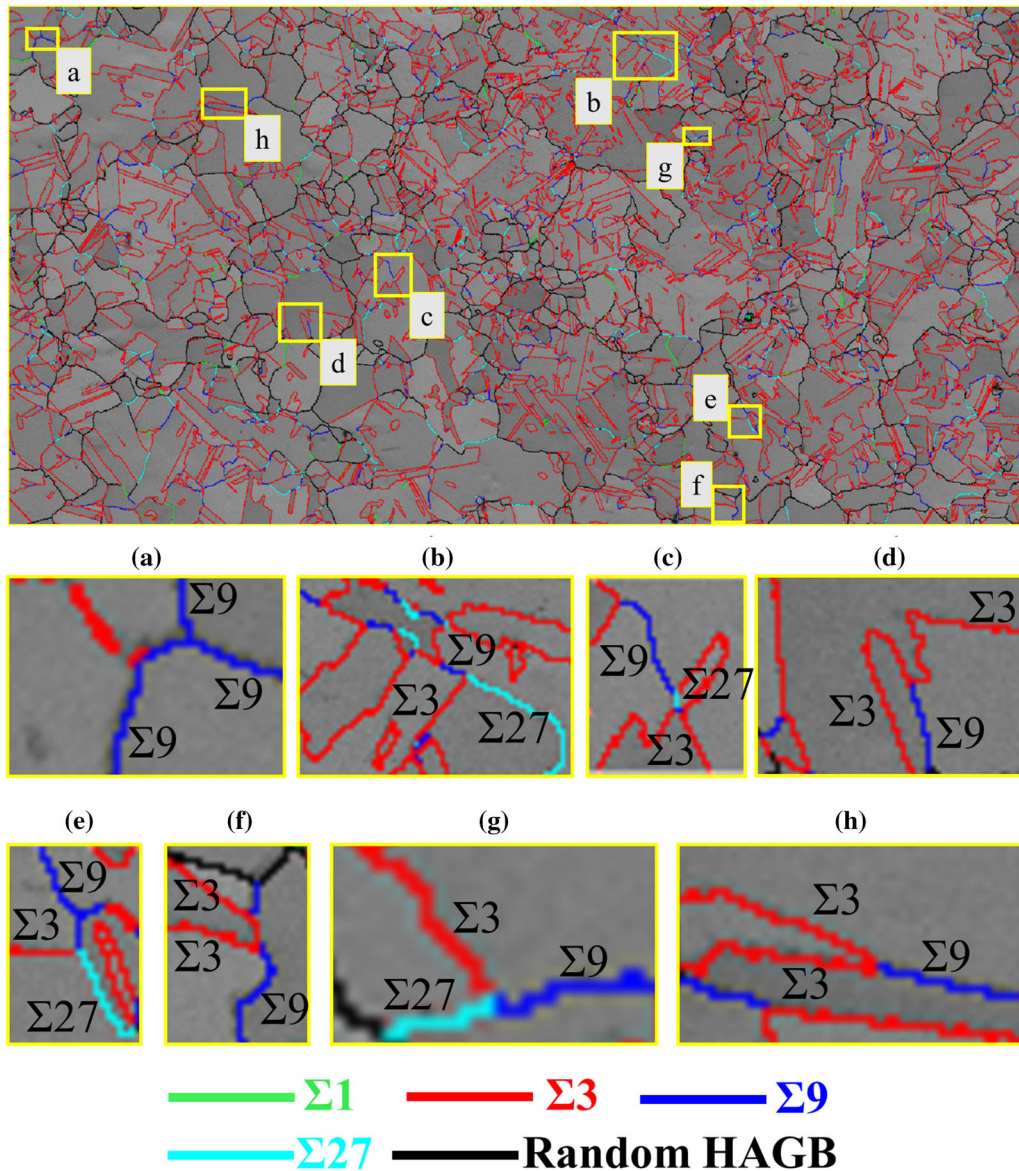


Fig. 11—OIM band contrast map overlaid with various kinds of grain boundaries for A3 sample condition, showing interactions of various  $\Sigma^n$  boundaries generated by the  $\Sigma^3$  regeneration mechanism. Reproduced with permission from Fig. 4 (A3): green:  $\Sigma 1$ , red:  $\Sigma 3$ , blue:  $\Sigma 9$ , aqua:  $\Sigma 27$ , and black: random HAGBs: (a)  $\Sigma 9 + \Sigma 9 = \Sigma 9$ , (b)  $\Sigma 3 + \Sigma 9 = \Sigma 27$ , (c)  $\Sigma 3 + \Sigma 9 = \Sigma 27$ , (d)  $\Sigma 3 + \Sigma 3 = \Sigma 9$ , (e)  $\Sigma 3 + \Sigma 9 = \Sigma 27$ , (f)  $\Sigma 3 + \Sigma 3 = \Sigma 9$ , (g)  $\Sigma 3 + \Sigma 9 = \Sigma 27$ , and (h)  $\Sigma 3 + \Sigma 3 = \Sigma 9$  (Color figure online).

the twin boundaries in the material. So, we have calculated the deviation for  $\Sigma 3$  boundaries corresponding to the various heat-treated samples using a parameter,  $\theta/\theta_m$ , that was calculated for  $\Sigma 3$  boundaries, where  $\theta$  represents the experimentally observed deviation and  $\theta_m$  denotes the maximum deviation allowed for the  $\Sigma 3$  boundary per the Brandon criterion (equal to 8.66 deg). Thus,  $\theta/\theta_m = 0$  represents the exact coincidence, while  $\theta/\theta_m = 1$  denotes the largest possible deviation per the Brandon criterion. As Figure 12 clearly shows, all the recrystallized samples (A0, A3, A4, A5, and A6) show a very high fraction of  $\Sigma 3$  boundaries (~94 pct) lying within the smallest deviation,  $\theta/\theta_m \leq 0.1$ . This deviation is approximately equal to our recently reported cut-off deviation of 1 deg in the case of recrystallized

microstructures.<sup>[20]</sup> Low deviation of the twin boundaries can also be gaged from the misorientation plot (Figure 6), which shows that the peak near misorientation angle 60 deg is very large and narrow in distribution for the A3 sample condition. This result shows that the character of twins in A1 and A2 sample conditions is very different from the other sample conditions. Again, a large deviation in twins' misorientation can be observed from their misorientation plots (Figure 6), which show that samples A1 and A2 exhibit a large spread of peaks near 60 deg misorientation; so, these twins are likely to have higher energy in comparison to the low deviation twin boundaries. This reaffirms our understanding that, although A1 and A2 show a high CSL fraction, these sample conditions may not display

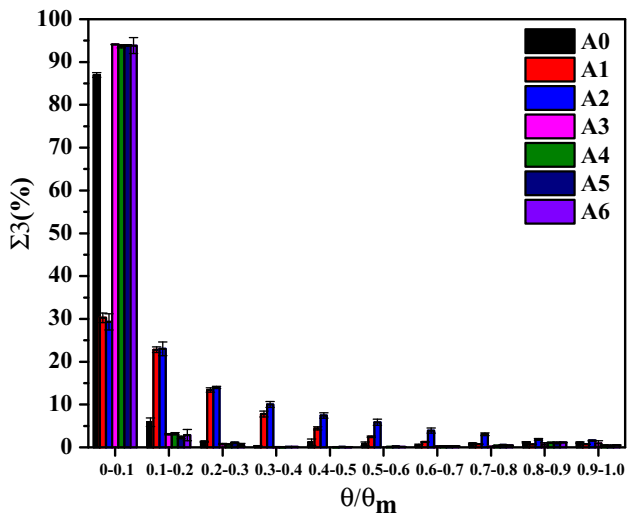


Fig. 12—Frequency distribution of  $\theta/\theta_m$  for  $\Sigma_3$  boundaries (Color figure online).

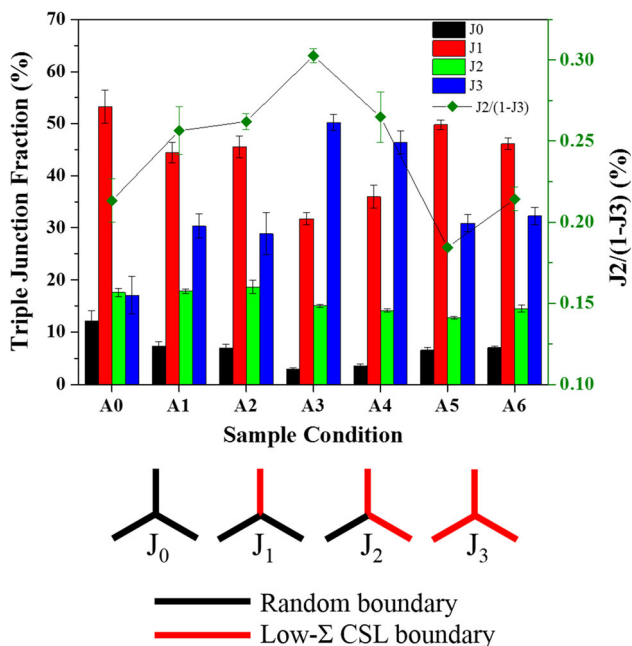


Fig. 13—TJD for various sample conditions (Color figure online).

improved grain boundary properties. A large fraction of  $\Sigma_3$  boundaries with small deviation is generally not found in the case of processing by cold rolling routes. This shows that hot rolling can be used to tailor microstructure in a way so as to generate low deviation  $\Sigma_3$  boundaries.

#### D. Triple Junction Analysis

##### 1. Triple junction distribution

As discussed earlier, a large fraction of special triple junctions ( $J_2$  and  $J_3$ ) is also required along with a large fraction of low- $\Sigma$  CSL boundaries, in order to obtain a truly engineered microstructure with enhanced properties. A variation in TJD for various sample conditions is

shown in Table III and plotted in Figure 13. On comparing various sample conditions for the types of triple junction fraction, we observe that, for all the sample conditions, except A3 and A4, the most populous triple junction fraction is  $J_1$ , which shows that the spatial distribution of low- $\Sigma$  CSL boundaries in the microstructure is relatively unclustered. For A3 and A4 sample conditions, the fraction of  $J_3$ -type triple junction is the highest. We see that there is a sudden rise of  $\sim 33$  and  $30$  pct in the fraction of  $J_3$  for A3 and A4 sample conditions, respectively, in comparison to that of A0. There is a considerable clustering of low- $\Sigma$  CSL grain boundaries in the microstructure to give the polarization toward  $J_3$ -type triple junction. Evidently, as the fraction of special boundaries increases, the fraction of special triple junctions also increases. This is consistent with the  $\Sigma_3^n$  regeneration mechanism and unequivocally proves that twin formation in sample conditions A3 and A4 is dominated by the regeneration mechanism.

Twins in sample conditions other than A3 and A4 were formed more by the new twin formation mechanism, which leads to lower fractions of  $\Sigma_9$  and  $\Sigma_{27}$  boundaries and, in turn, leads to a larger fraction of nonspecial,  $J_1$ -type triple junctions. The fraction of  $J_2$  is found to be small and relatively constant in comparison to  $J_1$  and  $J_3$  in all the sample conditions. This can be explained in terms of the geometrical constraints described by the addition rule, according to which if two CSL boundaries meet at a triple junction, the third interface must be close to another CSL boundary; hence, it will depend on the overall fraction of the low- $\Sigma$  CSL boundaries. Since the overall fraction of CSL boundaries is not very different for various sample conditions, the corresponding variation of  $J_2$  is also very small.

The junction of type  $J_0$  is considered undesirable from the point of view of breaking random structure. We observe that its fraction decreases from  $\sim 12$  pct in A0 to  $\sim 2$  pct in A3; it is also the least among all the conditions. Moreover, we observe a sharp rise in the fraction of most desirable,  $J_3$ -type triple junctions from  $\sim 17$  pct (for A0) to  $\sim 50$  pct for A3; also, it is the highest among all the sample conditions. On the other hand, the as-received sample, A0, had the highest fraction of  $J_0$  and least fraction of  $J_3$  (which is probably due to the least low- $\Sigma$  CSL fraction). In summary, we observe that, among all the sample conditions, A3 shows the most desirable distribution of triple junctions, which is expected to drastically reduce the grain-boundary-related degradation and failure.

##### 2. Grain boundary connectivity

Variation of the TJD can be better visualized in terms of the factor  $J_2/(1-J_3)$ , as plotted in Figure 13. This factor, as proposed by Kumar *et al.*,<sup>[22]</sup> is useful for assessing the effectiveness of the triple junctions in breaking the random grain boundary network. The microstructure having the highest fraction of  $J_2/(1-J_3)$  can be expected to show the least connectivity of the random grain boundaries network. This factor was introduced taking into consideration the fact that  $J_3$  is an ideal and stable triple junction where the failure front

has almost zero probability to approach. Thus, J2 refers to the special triple junctions that are least reactive during an intergranular degradation, and (1-J3) refers to that fraction of triple junctions that are active sites during an intergranular reaction. Thus, a high value of  $J2/(1-J3)$  in a microstructure can be expected to provide sufficient resistance toward an intergranular failure. From Figure 13, it is observed that the A3 sample condition has the highest value of  $J2/(1-J3)$ , suggesting it to be least reactive during any intergranular reaction.

The importance of TJE in GBE becomes obvious from Figure 14, which shows the network topology of various sample conditions. Here, random boundaries have been shown in comparatively thicker lines than those of the other boundaries, to have a better picture of the disruption of the random boundary network. The twins in A3 through A6 sample conditions consist mainly of straight and parallel-sided boundaries, which indicates that these are annealing twins and not deformation twins (the latter ones are not active in breaking the random boundary network).<sup>[4,50]</sup> In the case of A3,  $\Sigma 3''$  and other low- $\Sigma$  CSL boundaries can be seen to replace the random HAGBs, which helps in disrupting the connectivity of the random boundary network. It is clear from this figure that the random boundary network is very dense and interconnected for A1 and A2 sample conditions. This random boundary network is clearly disrupted for A3, A4, A5, and A6 sample conditions. Among these sample conditions, A3 and A4 clearly seem to be more effective. This improved behavior for these two sample conditions seems to arise from (a) the replacement of regular boundaries by special boundaries and (b) the formation of special junctions.

### 3. Correlation between the distribution of special boundaries and special triple junctions

From the foregoing discussion, it is now clear that the effective GBE cannot occur without TJE. However, it is

desirable that no additional processing step is needed for TJE. Hence, to understand the correlation between the evolution of the special boundaries and the special junctions, we plotted their distribution (Figure 15). Sample conditions A0 and A1 through A6 have been plotted on this map based on the values of the special boundary fraction and special junction fraction obtained using Brandon's criterion. We observe that the fraction of special junctions is approximately proportional to the fraction of special boundaries (with some scatter). Thus, the sample conditions leading to a very good fraction of special boundaries also result in a large fraction of special junctions. In other words, the processing conditions leading to GBE also lead to TJE.

To distinguish the extent of GBE and TJE in various sample conditions, we divided the plot area between special boundaries and special junctions into four

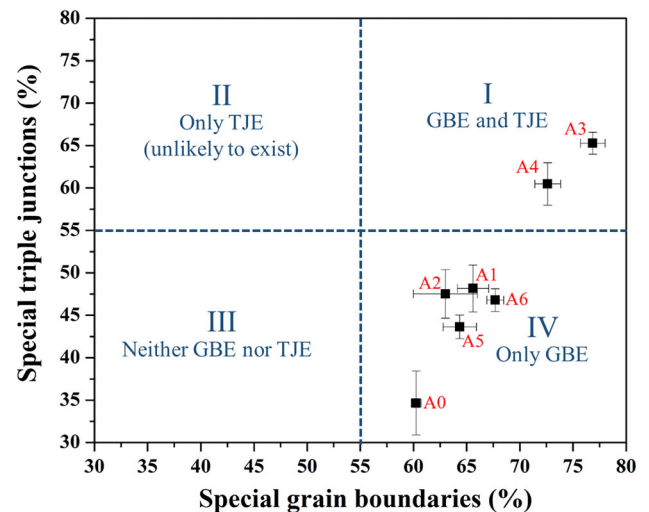


Fig. 15—Relationship between special grain boundaries and the special triple junction fraction (Color figure online).

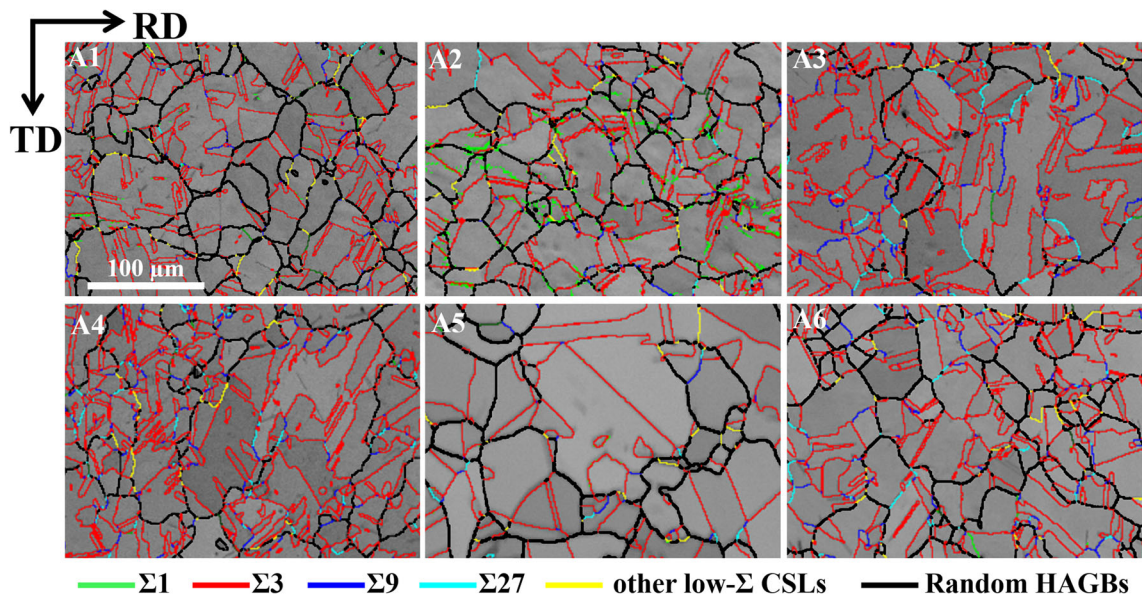


Fig. 14—Effect of TMP on the grain boundary network topology (Color figure online).

**Table III. TJD for Various Sample Conditions**

Sample Condition	J0 (Pct)	J1 (Pct)	J2 (Pct)	J3 (Pct)
A0	12.09 ± 2.00	53.25 ± 3.15	17.58 ± 0.75	17.09 ± 3.65
A1	7.41 ± 0.77	44.43 ± 1.99	17.83 ± 0.43	30.33 ± 2.32
A2	6.93 ± 0.80	45.56 ± 2.05	18.66 ± 1.24	28.86 ± 4.03
A3	2.96 ± 0.21	31.76 ± 1.15	15.05 ± 0.29	50.23 ± 1.56
A4	3.54 ± 0.38	35.99 ± 2.18	14.11 ± 0.33	46.36 ± 2.20
A5	6.58 ± 0.51	49.79 ± 0.92	12.73 ± 0.26	30.89 ± 1.63
A6	7.04 ± 0.30	46.17 ± 1.07	14.51 ± 0.64	32.28 ± 1.67

quadrants. Quadrant I indicates the high fraction of both special boundaries and special junctions, and it is the region where we can expect the best properties. We see that A3 and A4 sample conditions lie in this region and, thus, can be expected to show the best properties among all the processed samples. Quadrant 2 shows a hypothetical region having a high fraction of special triple junctions but a low fraction of special grain boundaries, which is unlikely to occur. Quadrant III shows a low fraction of both special grain boundaries and special triple joints, which is very likely to show substantial cracking during any intergranular degradation. Quadrant IV shows a region having a high fraction of special grain boundaries but a low fraction of special triple junctions. Most of the work to date related to GBE has concentrated on this region only, without investigating the triple junctions. We have shown that TJD is also an important parameter in obtaining an effectively engineered microstructure that can manifest into improved grain-boundary-related properties. Thus, this plot clearly distinguishes the characteristics of A0 and A3 sample conditions. Even though the A0 sample has a good fraction of special boundaries, it is not really a grain-boundary-engineered sample due to its very low fraction of special triple junctions.

## V. SUMMARY AND CONCLUSIONS

In this work, we explored the use of hot rolling as an economic and technologically easy-to-implement technique to improve the GBCD and grain boundary connectivity in polycrystalline materials. In this study, hot rolling followed by a short-time annealing step was used for GBE of Inconel 600 alloy. The effects of strain and poststrain annealing treatment on grain boundary evolution were investigated. At the temperature and conditions used, all samples underwent dynamic recrystallization; however, this alone was not sufficient to obtain any improvement in the GBCD. A postprocess static recrystallization was found necessary to improve the fraction of CSL boundaries. However, not all the statically recrystallized samples showed similar level of improvement. We found that a critical deformation (12 pct in this case) is necessary to obtain significant improvement in the GBCD. We conclude from our analysis that the optimal deformation must be sufficiently high to provide driving force for the postdeformation static recrystallization, yet low enough to retain a large fraction of original twin boundaries.

We further show that the deviation of CSL boundaries is another important criterion and only samples with a large fraction of CSL boundaries and with very low deviation from the exact misorientation can be considered to be “truly” engineered. Using this criterion, only statically recrystallized samples show a large fraction of low-deviation CSL boundaries. This also ensured that the fraction of LAGBs was negligible, as desired.

In addition to GBE, we were also able to achieve TJE, which ensures that the random boundaries network is significantly disrupted and any deleterious response of these boundaries does not proliferate for long distances into the sample. Coincidentally, the same sample for which we obtain effective GBE also showed the largest fraction of  $J2/(1-J3)$ . We showed in our analysis that both of these are related to the same two important factors: (1) a large fraction of original twin boundaries are retained, and this allows for (2) the  $\Sigma 3^n$  regeneration mechanism to be active in these sample conditions. These two factors ensure that we not only obtain the largest fraction of CSL boundaries but also the largest fraction of  $J2/(1-J3)$ .

This work clearly highlights that effective GBE can be obtained using an industrially feasible process, such as hot rolling. It should also be mentioned here that hot rolling and postdeformation annealing were carried out at the same temperature; hence, postdeformation annealing can be easily integrated with the deformation process. Based on the present results, the hot rolling process may potentially be exploited for GBE of other high-strength engineering materials.

## REFERENCES

1. T. Watanabe: *Mater. Sci. Eng. A*, 1993, vol. 166, pp. 11–28.
2. V. Randle: *Acta Mater.*, 1999, vol. 47, pp. 4187–96.
3. M.A. Arafin and J.A. Szpunar: *Corros. Sci.*, 2009, vol. 51, pp. 119–28.
4. F.J. Humphreys and M. Hatherly: *Recrystallization and Related Annealing Phenomena*, Elsevier, Oxford, United Kingdom, 2004.
5. T. Watanabe: *Res. Mech.*, 1984, vol. 11, pp. 47–84.
6. C. Cheung, U. Erb, and G. Palumbo: *Mater. Sci. Eng. A*, 1994, vol. 185, pp. 39–43.
7. E.M. LeHockey, G. Palumbo, and P. Lin: *Metall. Mater. Trans. A*, 1998, vol. 29A, pp. 3069–79.
8. Y. Gao, R.O. Ritchie, M. Kumar, and R.K. Nalla: *Metall. Mater. Trans. A*, 2005, vol. 36A, pp. 3325–33.
9. M. Detroy, J. Rotella, R.L. Goetz, R.C. Helmink, and S. Tin: *Mater. Sci. Eng. A*, 2015, vol. 627, pp. 95–105.

10. G. Palumbo and K.T. Aust: *Materials Interfaces*, Chapman and Hall, London, 1992, p. 190.
11. G. Hasson, J.Y. Boos, I. Herbeuval, M. Biscondi, and C. Goux: *Surf. Sci.*, 1972, vol. 31, pp. 115–37.
12. V. Randle: *Acta Mater.*, 2004, vol. 52, pp. 4067–81.
13. V. Randle: *Mater. Sci. Technol.*, 2010, vol. 26, pp. 253–61.
14. D.G. Brandon: *Acta Metall.*, 1966, vol. 14, pp. 1479–84.
15. L.C. Lim and R. Raj: *Acta Metall.*, 1984, vol. 32, pp. 1183–90.
16. H. Lin and D.P. Pope: *Acta Metall. Mater.*, 1993, vol. 41, pp. 553–62.
17. V.Y. Gertsman and S.M. Bruemmer: *Acta Mater.*, 2001, vol. 49, pp. 1589–98.
18. S.R. Ortner and V. Randle: *Scripta Metall.*, 1989, vol. 23, pp. 1903–08.
19. R. Joham, N.K. Sharma, K. Mondal, and S. Shekhar: *J. Mater. Process. Technol.*, 2017, vol. 240, pp. 324–31.
20. N.K. Sharma and S. Shekhar: *Philos. Mag.*, 2017, vol. 97, pp. 2004–17.
21. M. Winning, A.D. Rollett, G. Gottstein, D.J. Srolovitz, A. Lim, and L.S. Shvindlerman: *Philos. Mag.*, 2010, vol. 90, pp. 3107–28.
22. M. Kumar, W.E. King, and A.J. Schwartz: *Acta Mater.*, 2000, vol. 48, pp. 2081–91.
23. C.A. Schuh, M. Kumar, and W.E. King: *Acta Mater.*, 2003, vol. 51, pp. 687–700.
24. V.Y. Gertsman and K. Tangri: *Acta Metall. Mater.*, 1995, vol. 43, pp. 2317–24.
25. V.Y. Gertsman, M. Janecek, and K. Tangri: *Acta Mater.*, 1996, vol. 44, pp. 2869–82.
26. K. Mo, G. Lovicu, H.-M. Tung, X. Chen, Y. Miao, J.B. Hansen, and J.F. Stubbins: *J. Nucl. Mater.*, 2013, vol. 443, pp. 366–77.
27. V. Randle and A. Brown: *Philos. Mag. A*, 1989, vol. 59, pp. 1075–89.
28. W.E. King and A.J. Schwartz: *Scripta Mater.*, 1998, vol. 38, pp. 449–55.
29. G.S. Was, V. Thaveprungsriporn, and D.C. Crawford: *JOM*, 1998, vol. 50, pp. 44–49.
30. A. Vaid, K. Mittal, S. Sahu, and S. Shekhar: *Trans. Indian Inst. Met.*, 2016, vol. 69, pp. 1745–53.
31. P. Lin, G. Palumbo, U. Erb, and K.T. Aust: *Scripta Metall. Mater.*, 1995, vol. 33, pp. 1387–92.
32. M. Shimada, H. Kokawa, Z.J. Wang, Y.S. Sato, and I. Karibe: *Acta Mater.*, 2002, vol. 50, pp. 2331–41.
33. V. Randle and R. Jones: *Mater. Sci. Eng. A*, 2009, vol. 524, pp. 134–42.
34. W. Qiong, S. Da-le, L. Chang-sheng, and L. Chun-guang: *Eng. Fail. Anal.*, 2008, vol. 15, pp. 401–10.
35. D.C. Crawford and G.S. Was: *Metall. Trans. A*, 1992, vol. 23A, pp. 1195–1206.
36. C.B. Thomson and V. Randle: *Scripta Mater.*, 1996, vol. 35, pp. 385–90.
37. S. Kumar, B.S. Prasad, V. Kain, and J. Reddy: *Corros. Sci.*, 2013, vol. 70, pp. 55–61.
38. J.R. Crum: *Corrosion*, vol. 13, *ASM Handbook*, ASM, Materials Park, OH, 1992.
39. W.Z. Friend: *Corrosion of Nickel and Nickel-Base Alloys*, Wiley, New York, NY, 1980.
40. D.V. Rooyen: *Corrosion*, 1975, vol. 31, pp. 327–37.
41. L.C. Lim and R. Raj: *Acta Metall.*, 1984, vol. 32, pp. 1177–81.
42. V. Randle: *Mater. Sci. Technol.*, 1991, vol. 7, pp. 985–90.
43. F.J. Humphreys: *Scripta Mater.*, 2004, vol. 51, pp. 771–76.
44. M.C. Demirel, B.S. El-Dasher, B.L. Adams, and A.D. Rollett: in *Electron Backscatter Diffraction in Materials Science*, A.J. Schwartz, M. Kumar, and B.L. Adams, eds., Springer, Boston, MA, 2000, pp. 65–74.
45. H.-Y. Wu, F.-J. Zhu, S.-C. Wang, W.-R. Wang, C.-C. Wang, and C.-H. Chiu: *J. Mater. Sci.*, 2012, vol. 47, pp. 3971–81.
46. M. Caul, J. Fiedler, and V. Randle: *Scripta Mater.*, 1996, vol. 35, pp. 831–36.
47. D.P. Field, L.T. Bradford, M.M. Nowell, and T.M. Lillo: *Acta Mater.*, 2007, vol. 55, pp. 4233–41.
48. V. Gertsman: *Acta Crystallogr. Sect. A*, 2001, vol. 57, pp. 369–77.
49. H. Akhiani, M. Nezakat, M. Sanayei, and J. Szpunar: *Mater. Sci. Eng. A*, 2015, vol. 626, pp. 51–60.
50. V. Randle and G. Owen: *Acta Mater.*, 2006, vol. 54, pp. 1777–83.
51. A.J. Schwartz, W.E. King, and M. Kumar: *Scripta Mater.*, 2006, vol. 54, pp. 963–68.
52. D.J. Drabble, C.M. Bishop, and M.V. Kral: *Metall. Mater. Trans. A*, 2011, vol. 42A, pp. 763–72.
53. V. Randle, P. Davies, and B. Hulm: *Philos. Mag. A*, 1999, vol. 79, pp. 305–16.